

Measuring the scaling properties of temporal and spatial patterns: from the human eye to the foraging albatross

M.S. Fairbanks and R.P. Taylor

Physics Department, University of Oregon, Eugene, 97403, USA

To published as a book chapter in Nonlinear Dynamical Systems Analysis for the Behavioral Sciences: Real Data, published by Taylor & Francis

1. Introduction

Historically, the temporal behavior of many natural processes has been pictured as a game of extremes – nature appeared to be either highly ordered or highly disordered. Take the beating of the human heart as an example of order. A strong, regular beat was believed to be the signature of a healthy body. On the other hand, the gusts of wind in a passing storm were thought to be pure disorder – a random amalgamation of many events, all occurring at different rates and interwoven to create a vastly complex behavior as a function of time. In contrast to the heart, there was no regularity, no underlying pattern, to be found in the weather.

Over the past fifty years, the sophistication of equipment used to measure nature's processes has escalated, along with the computer power to analyze the resulting data, allowing scientists to peer beyond this simplified order-disorder view of the world around us. Many of nature's processes – both in our body and in our natural and social environments - have been found to consist of an intermediate balance between order and disorder. The healthy heart is now known to have fluctuations around a periodic beat [1], and the gusts of wind are not devoid of pattern [2]. In particular, many phenomena feature fluctuations that occur across many frequencies, where their contributions to the overall process follow a power law scaling relationship.

This power law establishes a type of uniformity across the various time scales. In particular, the data traces that chart the behavior as a function of time exhibit so-called 'scale invariance' or are referred to as 'scale-free'. Power laws do not feature a characteristic time scale. As a result, the data traces display similar characteristics over many time scales. This repetition across scales is also observed in many of nature's spatial patterns, where the analogous power law behavior is referred to as being fractal [3].

For both the temporal and spatial processes, the repetition of structure across many scales builds an immense complexity in the resulting pattern and this complexity is often central to the behavior of the system under investigation. Two parameters are important for quantifying the relative amounts of coarse (slow frequency) and fine (fast frequency) structure in the trace and the associated complexity - the exponent of the power law and the range of scales over which the power law holds. A traditional approach to determining these parameters is to perform a Fourier spectral analysis, in which the trace

is pictured as a summation of sinusoidal components and the amplitude of each component is plotted as a function of its frequency.

However, as fractal studies have spread through the research disciplines [3, 4], an alternative technique for assessing these parameters has gained momentum. This method is known generally as the “box-counting” technique and determines the above parameters by assessing the amount of area the data trace covers at different scales. In this chapter, we will demonstrate the relative strengths of the two techniques (Fourier and box-counting) and show that an integration of these two compatible techniques is a versatile approach for studying scale invariant processes in natural and social processes.

For the first part of the chapter, the two techniques will be applied to computer-generated traces to highlight their responses to idealized data. In the second part, we will move on to a physical system – movements of the human eye as a person looks at patterns projected on a screen. The human eye is chosen because it highlights the challenges of interpreting real data and also because this visual system simultaneously generates the two families of pattern discussed above. As the eye moves, the location of its gaze on the screen traces out temporal patterns: the horizontal and vertical co-ordinates of the gaze can each be plotted as a function of time and analyzed for invariance across time scales. At the same time, the trajectories linking the gaze locations trace out a spatial pattern that can be recorded and analyzed for invariance across size scales.

Finally, we will discuss the significance of the results of the scaling analysis for the performance of the eye – in particular, how scale invariance leads to an enhanced ability to search for information in nature’s fractal scenery. In this sense, the eye’s motion shares appealing similarities with the motions of foraging animals such as the albatross. In both cases, the main goal is to conduct a search that covers space efficiently. The eye’s search for visual information on a screen is analogous to animals searching for food. We will discuss how the mathematical properties of the power law scaling behavior achieve this through an inherent characteristic called enhanced diffusion.

2. A comparison of scaling measurement techniques for temporal patterns.

We start our investigation by considering the underlying methodology of the box-counting technique, as shown schematically in Figure 1 (a, b). The data trace represents a generic process in which a measured parameter (plotted on the y axis) evolves with time (plotted on the x axis) according to a process that features multiple frequencies. The traditional approach of employing a power spectrum analysis (a variant of Fourier analysis) to examine the frequency content of the trace is described in detail elsewhere [5]. The box-counting technique performs the same examination by covering the trace with a mesh of identical squares (‘boxes’) and counts the number of squares (shaded dark in Figure 1), N , that contain part of the data trace. This count is repeated for increasingly small squares within the mesh. In this approach, N assesses the amount of space covered by the trace at increasingly fine time scales (since the width of each square, L , has units

of time). A ‘scaling plot’ of $\log N$ plotted as a function of $\log (1/L)$ is frequently employed to investigate the scaling behavior of the data.

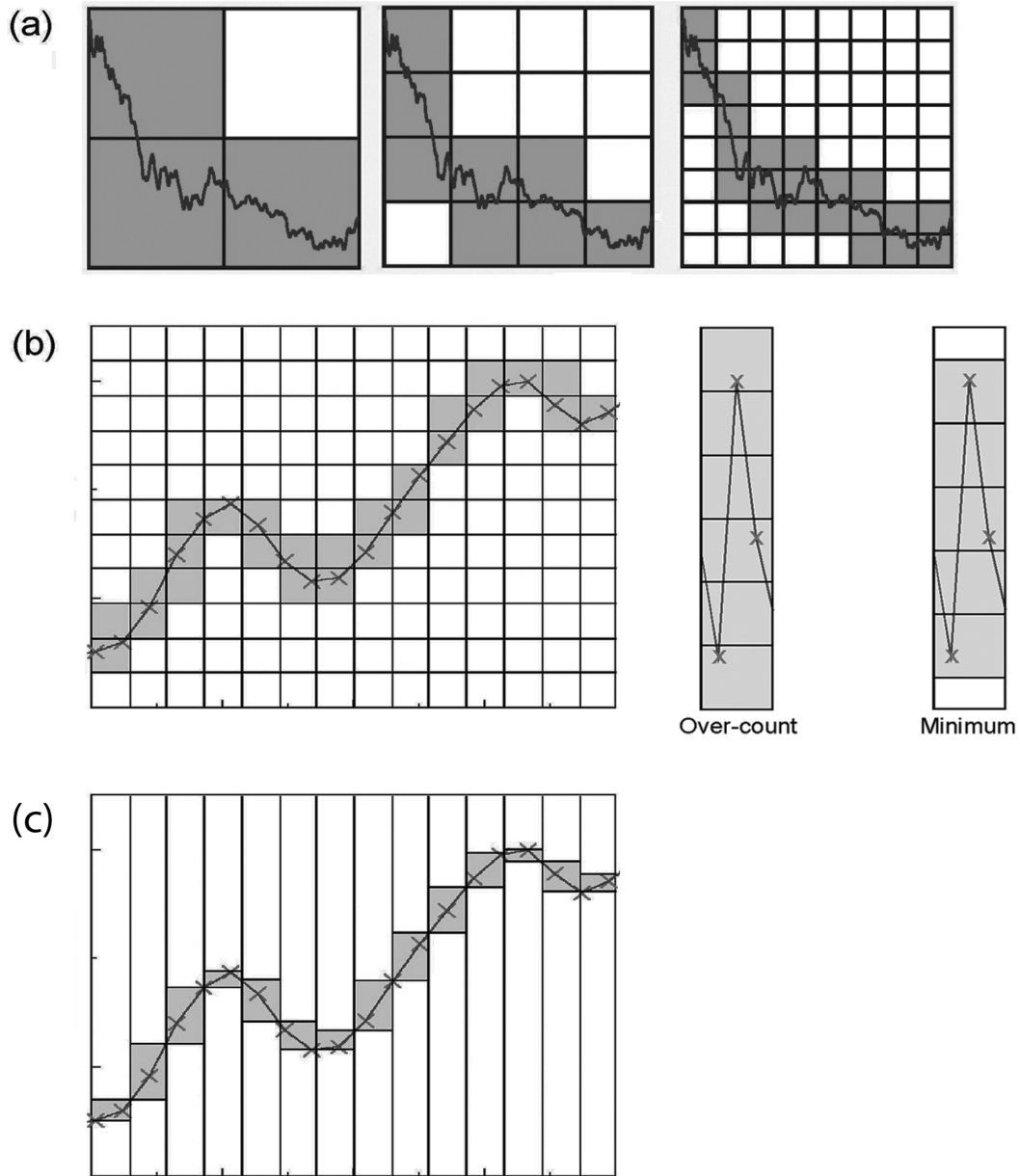


Figure 1. (a) shows 3 iterations of the box-count fractal analysis technique. A detailed single iteration is shown in (b) for an arbitrary profile, along with a schematic of how the box-count will often overestimate the box coverage of the profile. (c) shows the same profile measured with the variation method, showing a more accurate covering estimate.

Two magnification procedures are commonly adopted for constructing the scaling plots. For the first procedure, the square size L is reduced iteratively using the inverse expression $L = H/n$, where H is the trace length and n is the number of iterations ($n = 1, 2, 3 \dots$). For the second procedure, the exponential expression $L = HC^{-n}$ (where C is a

selected magnification factor) is applied iteratively. The first procedure has the advantage of generating a larger number of data points, while the second procedure reduces computation time and produces equally spaced points across the resulting log-log scaling plot.

This basic box-count algorithm has proven to be very popular for assessing both temporal and spatial patterns, in part because of its computational simplicity. However, it over-estimates the space coverage of the trace, as highlighted in Figure 1(b). The left-hand image shows an example trace at a chosen box size. The two right-hand images consider a small section of the trace and demonstrate that shifting the mesh vertically results in different counts (N values of 5 and 4 respectively). Consequently, one approach to minimizing the over-count would be to repeat the count for various shifts in the mesh position and to select the minimum N value obtained. Rotating the grid is an alternate approach that effectively provides both horizontal and vertical shifts.

An even more accurate method for minimizing the over-count is to adopt the variation method [6], which is shown in Figure 1(c) for the same scale considered in Figure 1(b). For this technique, columns replace the boxes. The height of the shaded area within a given column is determined by the difference of the heights at which the data trace enters and leaves the column. The total area (i.e. the sum of the shaded areas of all the columns across the whole trace) is then divided by the individual box area of Figure 1(b) to get the N value. Similar to the basic box counting technique, this is then repeated for increasingly narrow columns, and so assesses space coverage of the trace at increasingly fine time scales.

Figure 2 provides a comparison of this variation method (right-hand column) and the power spectrum analysis (middle column) for four simulations of time series data (left-hand column). The first row considers data that follows a simple line as a function of time t . The power spectrum analysis plots the power, $S(f)$, against frequency, f , and reveals a peak at zero frequency, as expected. The graph for the variation method plots N against $1/L$, where L is the column width. Since L is measured in units of time, the x-axis assumes a role analogous to frequency. The data is plotted on log-log axes to highlight that the data follows a power law of the form:

$$N \sim (1/L)^D \quad \text{Equation 1.}$$

In log-log space, this power law generates a straight line with a gradient equal to the exponent D . Measurement of the gradient reveals $D = 1$, highlighting the mathematical significance of the exponent – it represents the dimension of the data trace.

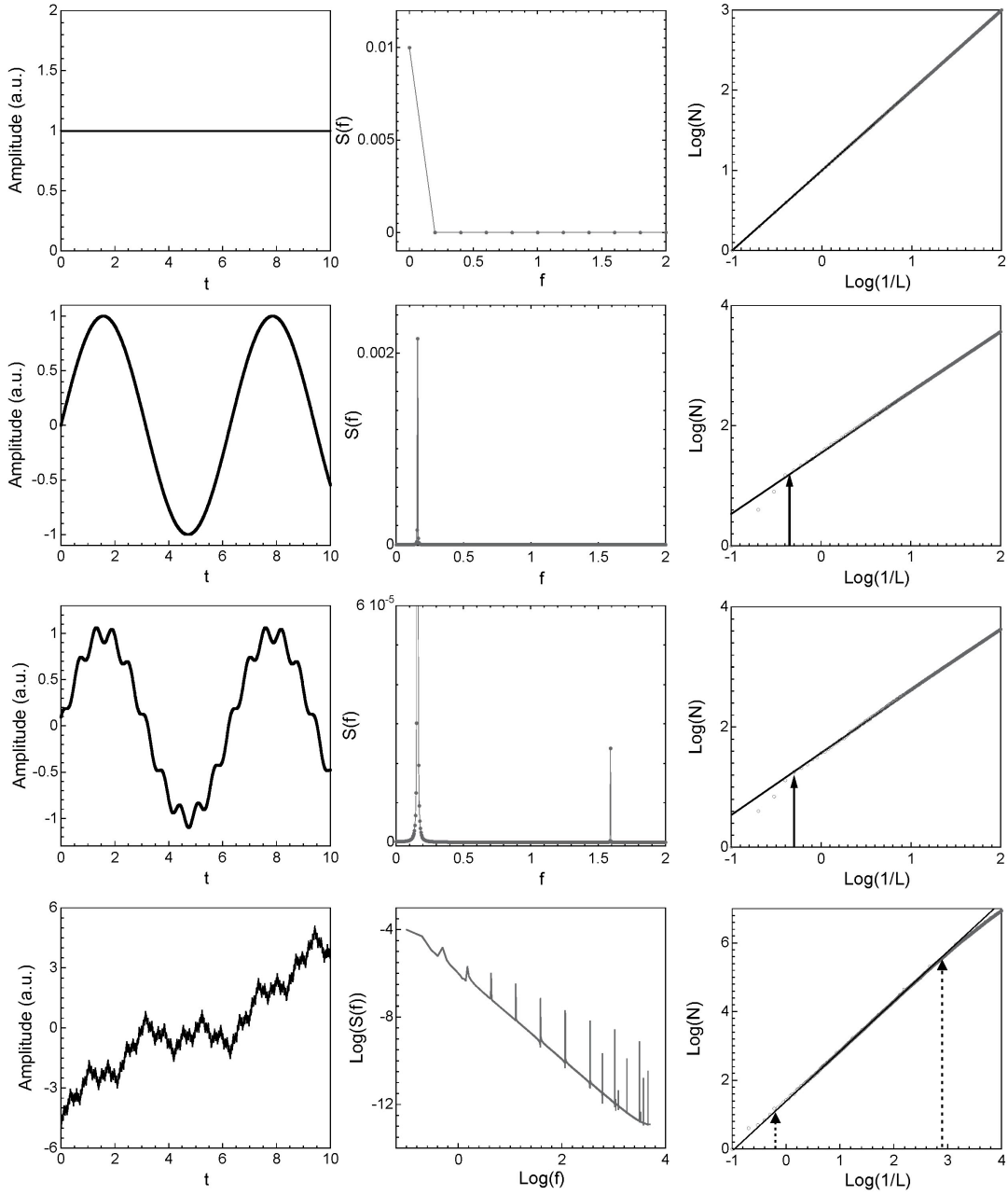


Figure 2. Each row shows a data trace (first column), its spectrum (second column), and the its scaling behavior using the variation method (third column). Arrows in the third column indicate where the scaling behavior ceases to hold. The fit lines (black) are fit to the entire data set in first three rows. In the fourth row, the line fits only to the data point in the scaling region between the indicated cutoffs (dotted arrows).

The second row of Figure 2 considers data that follows a sine wave as a function of time. As expected, the power spectrum analysis reveals a peak, corresponding to the inverse of the wave's period. The variation method again generates a straight line with $D = 1$ for small time periods (i.e. large $1/L$ values). This is a consequence of the fact that the narrow columns are sampling the smooth, one-dimensional character of the sine wave.

Only at wider columns (i.e. small I/L values) does the periodicity of the sine wave become apparent. This appears in the variation graph as a deviation of the data from the power law line, beginning at a scale indicated by the arrow.

A similar situation occurs for the third row, where a data set composed of two sine waves with different frequencies and amplitudes is considered. The power spectrum analysis reveals peaks at the two relevant frequencies. The variation method again deviates from the power law line. This deviation, indicated by the arrow, occurs at approximately the same I/L value as for the second row, because the additional, fast-frequency sine wave doesn't significantly affect the general form of the trace.

The data considered in the fourth row consists of a superposition of many cosine waves. The function is called a Weierstrass-Mandelbrot function, named after the mathematician who first studied this fractal form (Weierstrass) and Mandelbrot who generalized the function to make it analytically scale-invariant [7]. The amplitudes of the component waves scale with frequency according to the following power law:

$$W(t) = \sum_{n=-\infty}^{\infty} r^{-n(2-D)} (1 - \cos(r^n t)) \quad \text{Equation 2.}$$

To demonstrate the sensitivity of the power spectrum analysis to this fractal power law relationship, we have plotted the results of the power spectrum analysis in log-log space. The peaks clearly occur at even intervals of $\log(f)$, with the peak heights falling off according to the straight slope expected of the power law.

Whereas the power spectrum analysis follows expectations, the variation graph of the Weierstrass function reveals an intriguing result – the data once again follows a straight line, but the D value determined from the slope has lifted from its integer value and now assumes the value of 1.5. If we maintain the same physical interpretation as before (that the slope measures the dimension of the data) then this signifies that the Weierstrass function has a non-integer dimension. Indeed, this quality is a defining characteristic of fractals. The ‘covering’ dimension (extracted by covering assessment techniques such as the variation method) of a fractal trace must be higher than the topological dimension (which is one dimensional, since the data is strung together to form a line rather than, for example, a zero dimensional dot or a two dimensional area). An intuitive mathematical interpretation of this result is that the repeating structure embedded in the line causes it to start to occupy area, but not to the extent of filling the two dimensional plane. This is reflected by a covering dimension that lies between 1 and 2.

Another important result, highlighted by Figure 2, is that the fractal power law does not extend to infinitely small nor infinitely large frequencies. This restriction is due to the limits of measurement resolution. At the highest frequencies (i.e. large values of I/L), the narrowing column widths start to approach the data resolution limit. The scaling behavior of the data then deviates from the fractal power law and the data no longer follows the straight line, as indicated by the right-hand arrow in the variation graph. At the low frequencies (i.e. small values of I/L), the column width starts to approach the length of

the trace and the number of columns becomes severely restricted. The resulting limitation in counting statistics causes the data to deviate from the straight line. In particular, the low number of columns hinders the technique from distinguishing the fractal line from a filled two-dimensional space, with the consequence that the filled columns generate a line with a gradient approaching $D = 2$.

These ‘cut-offs’ (indicated by the two arrows) limit the frequency range over which the fractal power law behavior is observed. It should be stressed that the frequency range *does not* feature inherently in the definition of a fractal. However, a limited range impedes the confidence level of determining if the line is in fact straight (for example, many functions can appear straight over one order of magnitude when plotted on a log-log graph) and also limits the level of accuracy in determining D from the line’s slope. As an empirical guide, column widths narrower than five data points should be excluded from fractal analysis. This is also true of columns with widths larger than one fifth of the length of the trace itself (for experimental data, one tenth is often used). These measurement requirements set the frequency range observed in Figure 2. For this mathematically-generated fractal, the ‘upper’ (i.e. high frequency) cut-off could have been extended by reducing the data point separation. Similarly, the ‘lower’ (i.e. low frequency) cut-off could have been extended by generating a longer trace. For experimental data, more limiting considerations also factor into determining these cut-offs and we will return to this discussion in the next section.

It should be noted that experimental traces rarely have the exact pattern repetition observed in these simulated traces. This rather artificial form of fractal scaling is highlighted in Figure 3 (left column) by repeatedly magnifying one section of the trace, revealing an exact repetition of the structure at increasingly fine time scales. Because of this exact repetition, the function is labeled as an exact fractal. The right column shows another form of fractal referred to as a statistical fractal. For this fractal, the pattern doesn’t repeat exactly. Instead, only statistical qualities repeat, with the consequence that the pattern looks similar at different magnifications.

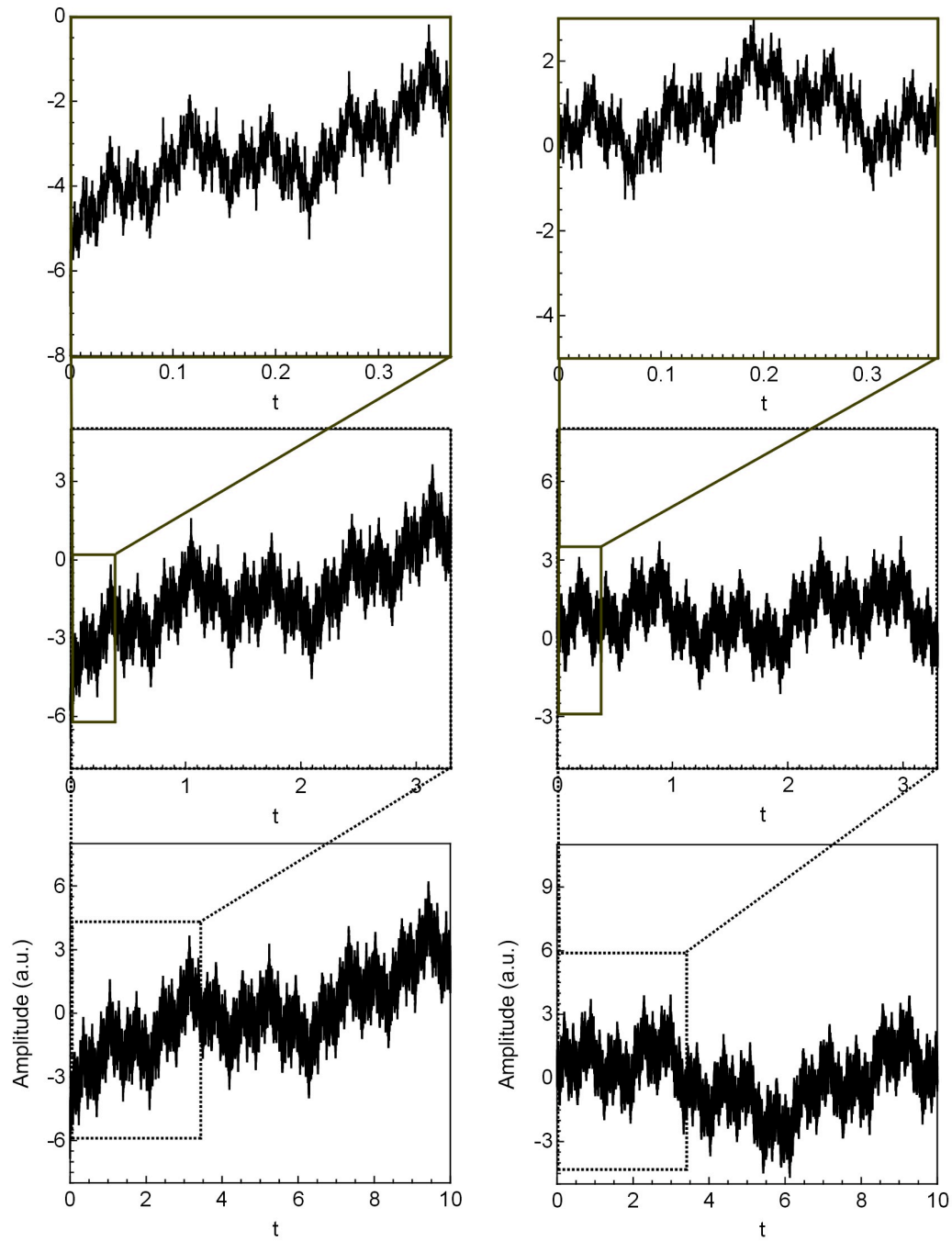


Figure 3. Two sets of Weierstrass fluctuations with exact self-similarity (left column) and statistical self-similarity (right column). The generating function is identical in each case except for the addition of a random phase to each sinusoidal component in the statistical case.

This statistical form of the Weierstrass function was generated by using Equation 2 but randomizing the phases of the various cosine waves. This randomization preserves the power law behavior, and hence the basic fractal quality, of the trace. Thus the power spectrum and variation graphs are very similar to those for the exact fractal shown in

Figure 2. Many natural (temporal and spatial) processes generate statistical fractals because of nature's integration of randomness with an underlying power law scaling behavior. Because of the role of randomness, these fractals are also sometimes referred to as random or stochastic fractals.

We are now in a position to consider how the two important parameters of power law behavior – the frequency range and the power law exponent – compare for the two measurement techniques. The observed scaling range of the fractal is determined by the cut-offs discussed above, and these occur at approximately the same frequencies for the two methods. How, though, do the slopes of the fractal power laws extracted by the two analysis methods compare? This is considered in more detail in Figure 4, where 3 Weierstrass fractal traces are generated in the left figure with D values of 1.2, 1.5 and 1.8. The middle figure shows the associated analytical power spectrum behavior, where the data points indicate the peak amplitudes (determined using Equation 2). The values of these peaks drop off according to the following power law:

$$S(f) \sim f^{-\alpha} \quad \text{Equation 3.}$$

Thus the gradient is $-\alpha$ for the log-log graph shown in Figure 4 (middle). The right-hand graph of Figure 4 shows the variation graph. This graph charts the behavior $N \sim (1/L)^D$ (see Equation 1). Therefore, the gradient is D for the log-log graph shown. Although its derivation is beyond the focus of this chapter, D and α are linked by the following mathematical relationship (Note: this relationship is derived for a fractal generated using fractional Brownian statistics) [8]:

$$D = (5 - \alpha) / 2 \quad \text{Equation 4.}$$

Note that, for a temporal trace to be fractal, D must have a fractional value lying in the range $1 < D < 2$, and so the corresponding α must satisfy $1 < \alpha < 3$.

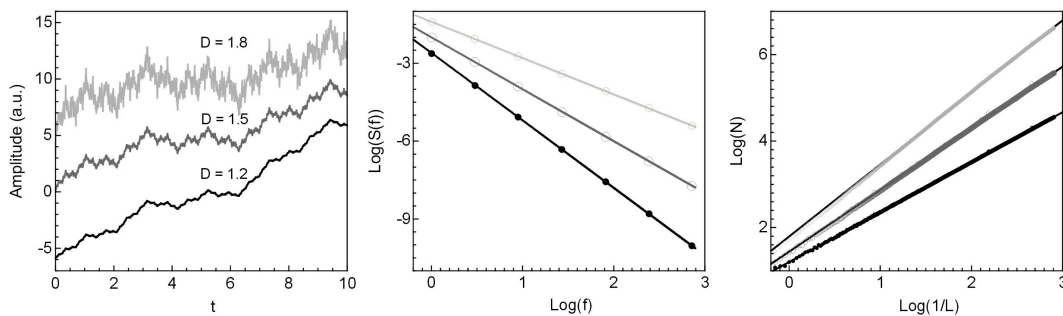


Figure 4. Three sets of Weierstrass fluctuations with differing D values (left panel), the associated analytical power spectra (center), and the results of the variation method (right) for each set. The analyses are only plotted over the region where the scaling behavior holds. The data points on the power spectra indicate the positions in frequency of the Weierstrass' constituent sinusoids.

It is informative to check that the inverse relationship between D and α , revealed both in Equation 4 and Figure 4, agrees with intuition. First consider the 3 traces of the power spectrum graph (middle column). The α value determines the fall-off in the power of the

cosine wave components when moving to higher frequencies. Thus a larger α value will lead to a lower power at high frequencies. This can be seen in the Weierstrass traces (left column): high frequency structure is less dominant in the trace with the higher α value (bottom trace). Now consider the variation graph (right column). The D value sets the rate at which N increases as the column size L is reduced. A higher D trace will therefore have a higher N value at large $1/L$ values, translating to there being more fine structure in the high D trace than an equivalent low D trace. This can be seen in the 3 Weierstrass traces.

Whereas Equation 4 provides the mathematical relationship between D and α , the values of D extracted from the variation scaling plots are often found to be less than the values calculated from α using Equation 4. What is the source of this discrepancy? Figure 5 addresses this question by returning to the issue of cut-offs and the associated frequency range. This figure shows the result of a variation analysis performed on 3 Weierstrass traces, where the analytical D value from Equation 2 is 1.5 but the frequency range over which this power law is obeyed varies.

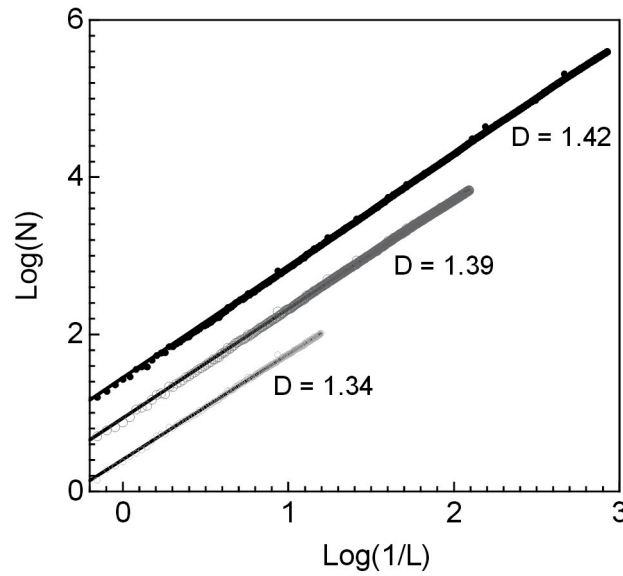


Figure 5. A comparison of variation method scaling plots for three sets of Weierstrass fluctuations. The analyzed data sets were generated with 3, 4, and 5 orders of magnitude in data resolution with fractal power law scaling over the plotted ranges.

It is clear that, as the frequency range increases, the accuracy of the D value measured from the gradient rises toward the input value. For the trace where the fractal power law holds for 3 orders of magnitude in frequency, the measured value of 1.42 almost matches the input value of 1.5. Table 1 shows similar results for different values of input D values of 1.2, 1.5 and 1.8. In each case, increasing the range of frequencies results in a more accurately measured D value.

Analytical Dimension	Dimension (1.4 orders)	Dimension (2.3 orders)	Dimension (3.1 orders)
1.2	1.12	1.14	1.15
1.5	1.34	1.39	1.42
1.8	1.57	1.62	1.67

Table 1: A summary of the measured D values obtained from the variation method for fractal traces with different scaling ranges. The left column shows the D value used to generate the traces, whereas the right three columns show the measured values.

Figure 6 considers a further approach to improving the accuracy of the box-counting method. The Horizontal Structured Elements (HSE) method also assesses the coverage of the data trace but does so in a different manner than the box-counting and variation methods. The HSE method places a mesh of squares over the trace with a width L_R that typically matches the data resolution. Squares in the mesh that contain part of the data trace are assigned a value of 0. Values are assigned to other squares based on their horizontal distance to the nearest square of value 0. In other words, if a square is next to a square of value 0 it is assigned a value of 1, if it is the next square along it is assigned a value of 1 and so on, as demonstrated in the schematic representation of Figure 6(a). Once the distance values have been assigned, a count is made, firstly of the number of squares of value 0, $N(0)$, then of the number of squares of value 0 or 1, $N(0,1) = N(0) + N(1)$, and so on. Although beyond the scope of this chapter, it can be shown [6] that the following equation can be used to calculate $N(L)$:

$$N(L) = (L_R)N(0,1,2, \dots k)/L^2 \quad \text{Equation 5.}$$

where $L = (k - 1)L_R$. Thus it is possible to plot the usual scaling plot of $\log(N)$ against $\log(1/L)$ and obtain a straight line with the gradient given by D .

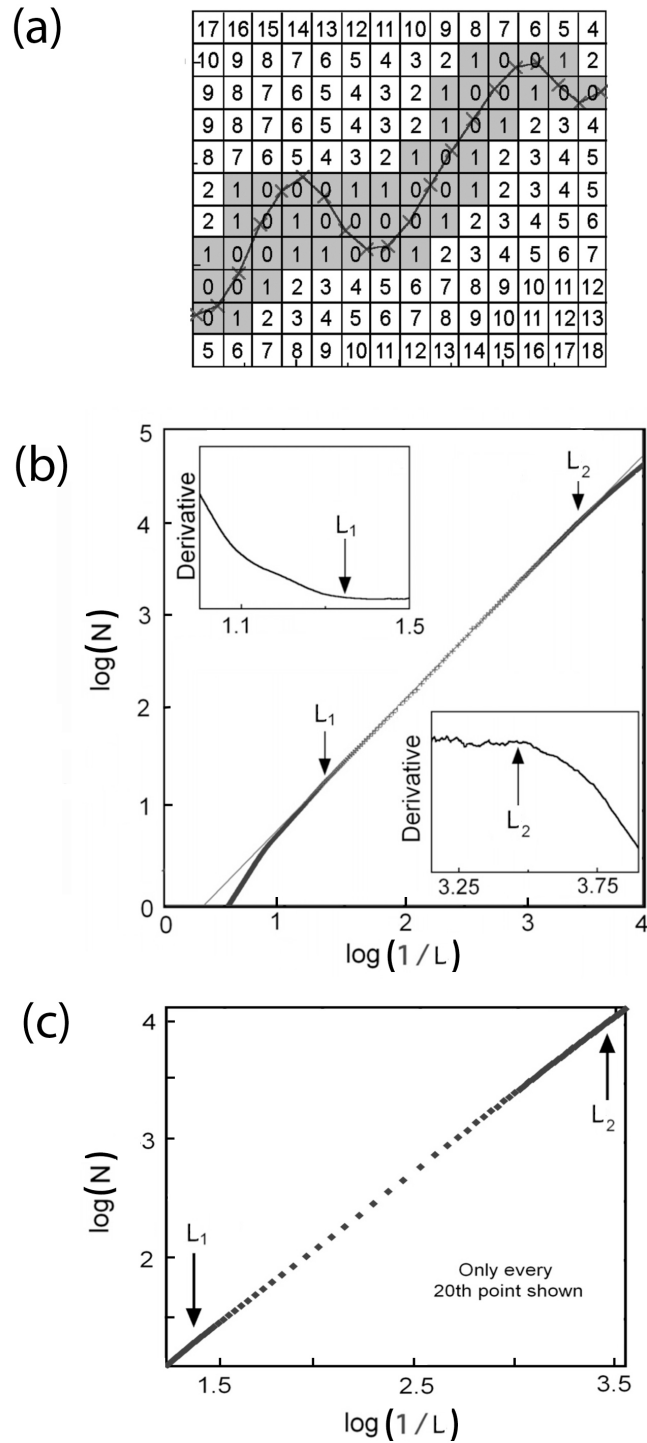


Figure 6. A demonstration of a more detailed fractal analysis on a generic data trace. (a) shows a schematic of the horizontal structured elements (HSE) analysis method. In combination with the variation method, the analysis gives a scaling plot with high data densities over all size scales (b), which enables derivative analysis to detect the appropriate cutoffs (insets). (c) shows only the power law scaling region with the calculated cutoffs L_1 and L_2 .

A crucial feature of the HSE method lies in the distribution of the data points in the resulting scaling plot. Instead of having an increasing data point density in the high ($1/L$) direction (as is the case for the basic box-counting and variation methods when using the magnification equation $L = H/n$ discussed above), the data point density of the HSE method is highest at the small ($1/L$) end of the scaling plot. This difference in the point distribution between the variation and the HSE methods is exploited in Figure 6(b), where the data from the two methods has been combined in one scaling plot. As shown more clearly in Figure 6 (c), where only every twentieth data point has been shown, this provides a high data point density across all frequencies. This high density is sufficient to apply a derivative analysis to detect the frequency values of both the upper and lower cut-offs, as shown in the insets of Figure 6(b). This more accurate location of the cut-offs (marked L_1 and L_2 in the insets), combined with the increased data density between the cut-offs, improves the accuracy of the fit to the data and thus the D value extracted from the fit.

3. Scale analysis of a physical system – the motions of the human eye.

We now move on to investigations of data generated by physical systems. The temporal behavior of many natural systems has been successfully quantified using power laws, spanning the physical, natural and social sciences [3, 4]. A common nomenclature has emerged across these disciplines to categorize the scaling behavior of systems according to the scaling exponent α , as summarized in Table 2:

Name	White	Pink	Brown	Black
α	0	$0 < \alpha < 2$	2	> 2
D	2	$2 \leq D < 1.5$	1.5	> 1

Table 2: A summary of α and D values for the common categories of power law scaling behaviors.

This nomenclature is based, in part, on analogies with the color spectrum of light. For example, white power laws have equal power at all frequencies, analogous to white light featuring contributions from all visible frequencies. Pink power laws have a higher α value, indicative of an increase of power at lower frequencies (see Figure 2 for example), analogous to pink light. Brown (so named because time series data generated from Brownian random statistics are quantified by $\alpha = 2$) and black power laws have even higher α values. The third row of Table 2 shows the D value obtained using Equation 4.

While discussing Table 2, it is opportune to return to our earlier definition of fractals: for time series data, the D must have a fractional value lying in the range $1 < D < 2$. This restriction arises because the D value must be higher than the trace's topological value (which equals 1) but cannot exceed the dimension of the graphical space that the data is embedded into – the so-called embedding dimension (which equals 2). For this reason,

white power laws have $D = 2$, and not greater, because it is confined to a two-dimensional plane.

Note that the D values listed in Table 2 describe the dimensions of the temporal data traces. If these temporal processes correspond to an object moving through space, then the spatial pattern generated by the spatial trail will have a D value given by the following relationship (this relationship is derived for the fractal process fractional Brownian motion)[8, 9]:

$$D = 2 / (\alpha - 1) \quad \text{Equation 6.}$$

Note also that it is possible for the temporal trace to be fractal and the equivalent spatial pattern not to be fractal. This occurs, for example, with Brownian processes ($\alpha = 2$). The temporal trace is quantified by $D = 1.5$, while the spatial data is quantified by $D = 2$. So called fractional Brownian processes ($\alpha > 2$) are a good example where both the temporal and spatial patterns are fractal. We will return to this difference between Brownian and fractional Brownian motion in the discussion section.

Let us now consider the physical significance of the α value of the temporal trace. A high α value (and corresponding low D value) indicates a bias toward components with long time periods. For biological, physiological or social systems, this increased correlation across long time scales implies a ‘memory’ within the system. At the other extreme of scaling behavior, white power laws describe systems with no memory – there is no correlation between events and processes occurring at different times.

What, then, is the correlation - the ‘color’ and dimension - of a physiological system such as the human eye? Not surprisingly, this will depend on the task being performed by the visual system. Whereas the gaze behavior when looking at figurative stimuli such as the human body or human faces has been the subject of much research [9], the gaze patterns activated by more abstract visual stimuli is considerably more subtle and less understood. In particular, until recently it has been unclear what happens when the eye goes into ‘search mode’, seeking out valuable information embedded, or even hidden, in a clutter of highly complex background information. How does the eye search?

Figure 7 shows an example of the spatial (a) and temporal (b) patterns traced out by the human eye when in search mode. The data was recorded using the eye-tracking equipment shown in Figure 8. This “eye-gaze system” (from LC Technologies) integrates infrared and visual camera techniques to determine the location of the eye’s gaze when looking at a pattern formed on a computer screen [10]. This remote tracking is unobtrusive (requiring no attachments to participants) and is functional for a range of participants, including those wearing contact lenses and glasses. The sizes of the images on the screen were 290mm by 290mm, corresponding to 1024 by 1024 screen pixels (i.e. the image resolution was 35.3 pixels per cm). The eye-tracker can locate the gaze with an accuracy of 4 pixels. The distances traced out by the gaze on the screen can be converted to the corresponding change of the eye’s viewing angle using the separation distance between the eye and the screen (which was 0.56m).

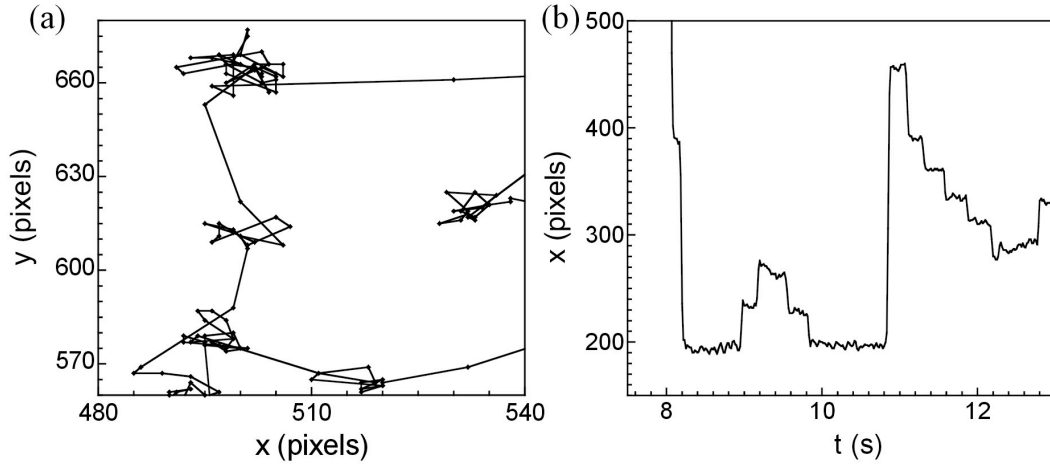


Figure 7. Subsections of a single eye-tracking data set: the spatial pattern (a) and the times series x vs. time (b).

Figure 7(a) shows a magnified section of one region of the spatial pattern traced out by the eye's gaze as it moves across the screen. As expected, the pattern is composed of long ballistic trajectories as the eye jumps between the locations of interest, and smaller motions called micro-saccades that occur during the dwell periods to ensure that the retina does not de-sensitize [10]. Figure 7(a) plots the horizontal (x) and vertical (y) locations of the gaze in units of screen pixels. Micro-saccades are expected to occur over an angular range of typically 0.5° . This angle translates to a distance of 15 pixels on the screen and, as expected, this approximately matches the typical width of the dwell regions observed in Figure 7(a). Given that the saccades and micro-saccades are produced by different physiological mechanism and serve different purposes within the visual system, it is expected that their scaling behaviors will be different. The scaling analysis of the spatial patterns will therefore be expected to reveal a crossover between the two processes – the saccades and micro-saccades – at a size scale of approximately 15 screen pixels.

Figure 7(b) shows the corresponding temporal pattern by plotting the x position against time t . The periods of relative motionlessness are the dwell periods at a given location, during which time the eye is undergoing micro-saccades. The typical dwell time is approximately 0.4s. The time scale of the individual micro-saccades is expected to be approximately 10-20 milliseconds. We note that this is on the same order as the sampling rate of the eye-tracking equipment (16ms, 60 Hz). This measurement limitation would therefore impact on any studies of the micro-saccades. However, the focus of our investigations lies with the saccades, since these larger motions are the ones that dictate the search motion, and these operate on longer time scales than the equipment's sampling rate. The basic form of the temporal trace observed in Figure 7(b) occurs over time scales of interest (i.e. times longer than the micro-saccades and longer than the equipment resolution limit) and is formed by an interplay between dwell periods and ballistic jumps.

Recent experiments, using a similar experimental set-up to that of Figure 8, investigated the temporal patterns when observers were asked to search for visual icons embedded in a visually complex pattern on a computer screen. These temporal patterns followed a power law scaling behavior [11].



Figure 8. A photograph of one of the authors (MSF) using the eye-tracking apparatus.

We have built on this intriguing result by investigating the temporal behavior as the eye searches through the visual complexity of a fractal pattern. Figure 9 (left column) shows the underlying fractal patterns (light gray) that were displayed on the computer screen. The dark trajectories are the saccades of the observer's eye during an observation period lasting 60 seconds. In each case, the observer was instructed to memorize the pattern in order to induce the search activity. The D values of the displayed monochrome fractal patterns were 1.11 (top), 1.66 and 1.89. The fourth image (bottom) is a composite of four differently colored interlocking fractal patterns, each with a D value of 1.6. All of the fractal images are taken from paintings created by the artist Jackson Pollock (the significance of which will be discussed in more detail below).

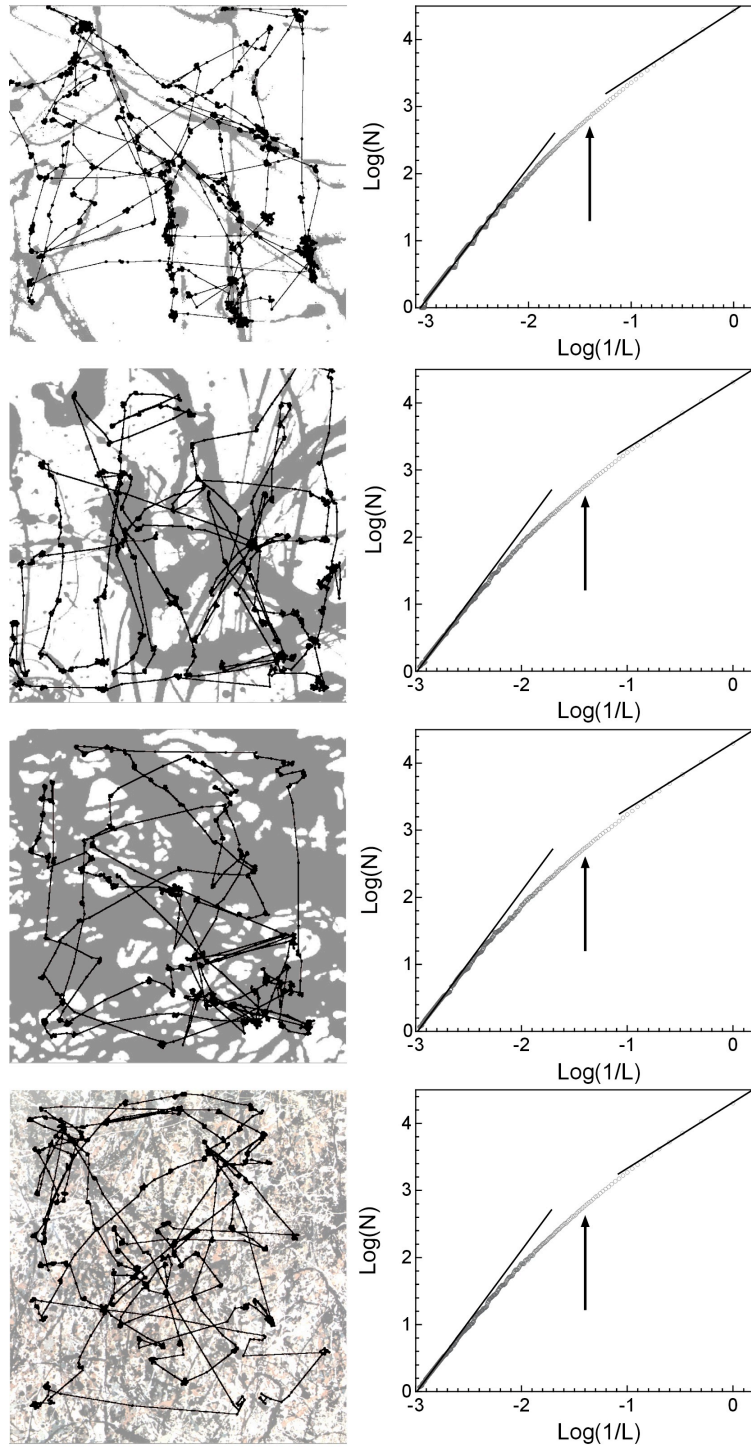


Figure 9. The complete spatial eye-tracking data sets (left column) and their associated box-count scaling plots (right). The eye-tracks are overlaid on the observed fractal patterns, which have dimensions of $D = 1.11$ (first row), $D = 1.66$ (second), and $D = 1.89$ (third). The final pattern is a colored composite of four $D = 1.6$ patterns. The scaling plots show the entire box-count data set with typical fixation size (arrows), $D = 1$ (right-hand line), and $D = 2$ (left-hand) trends.

The right-hand column features the scaling plots resulting from the spatial analysis of the saccades. However, we first concentrate on the analysis of the associated temporal patterns, as shown in Figure 10. The left column shows the time series traces, together with the spectral analysis (middle column) and box-counting analysis (right column). For both forms of analysis, the scaling plots examine the scaling behavior between the lower (slow frequency) and upper (fast frequency) cut-offs. In each case, as a guide we have indicated the typical dwell time (0.4s) with an arrow. The cut-offs correspond to the time scales of 5s and 80ms. These are set by the same measurement principles outlined earlier for the simulated Weierstrass function: 80ms corresponds to being 5 times larger than the resolution limit (set by the equipment's sampling rate of 16ms) and 5s corresponds to being one tenth of the length of the trace (set by the observation period of 60s).

However, whereas the observation range of the simulated fractal traces could be expanded by increasing the data resolution and the length of the trace, this is not the case for the experimental data of Figure 10. Even if the equipment sampling rate were to be increased (the latest eye-trackers can sample at 240Hz), the experiment would be measuring a different physical process at these fine time scales, one dominated by the micro-saccades. Similarly, if we were to lengthen the data trace by increasing the observation period, a different physical process would again take over – after 60s, observers lose concentration and their gaze tends to wander off screen.

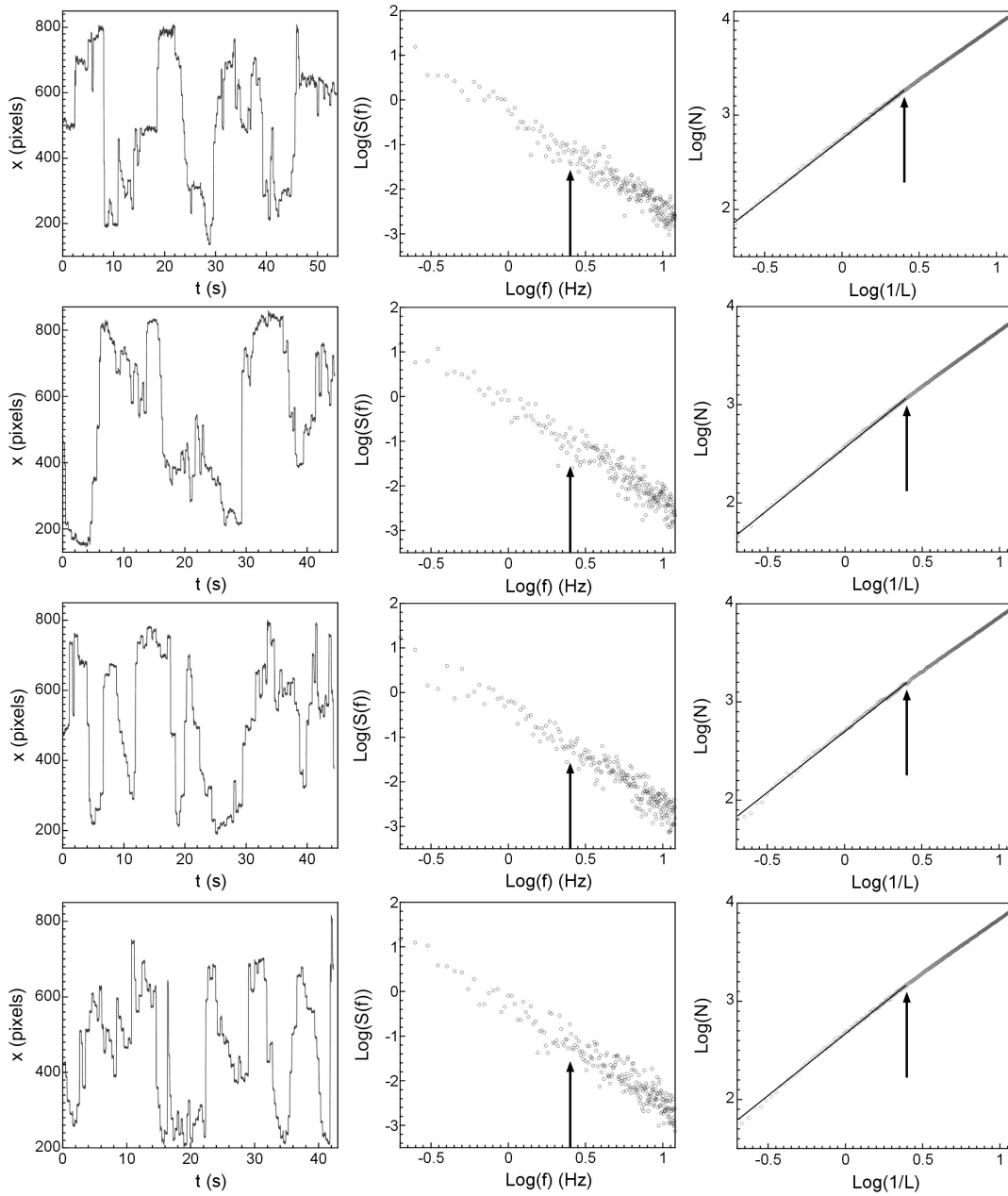


Figure 10. Time series of position x vs. time (left column) for each of the eye-tracks pictured in Figure 9 with corresponding power spectrum (center) and variation method (right) analyses. Arrows indicate the typical fixation time length (~ 0.4 s) on each scaling plot. Fit lines of uniform gradient show the region of strict power law scaling in each variation method plot.

These factors highlight a crucial characteristic of physical fractals. Unlike their mathematical counterparts, physical processes have inherent upper and lower cut-offs in addition to the measurement cut-offs. For this reason, physical fractals are often referred to as ‘limited range fractals’. The magnification range of nature’s physical fractals is surprisingly small – the typical range is only 1.25 orders [12]. For this reason, it is not always clear whether a data trace is actually fractal, or if the data is simply mimicking the

power law behavior for a limited magnification range. Nevertheless, the gradient of the scaling plots can still be effective in quantifying the relative contributions at different frequencies. In such as case, we refer to the D value extracted from the gradient of the scaling plot as being an “effective dimension” to highlight this ambiguity.

We note that the power spectrum scaling plots of Figure 10 are inherently more noisy than the equivalent box-counting plots. For this reason, we take the effective dimension measured from the box-counting plots ($D = 1.2$), and use Equation 4 to calculate the equivalent α value (2.6). We note that we expect this D value to be an under-estimate of the actual value due to the limited magnification range (see the earlier discussions on the Weierstrass function). It is interesting to compare this result to the experiment where observers were asked to search for embedded icons, where $\alpha = 2$, extracted directly from the power spectrum analysis, indicated Brownian power law behavior [11].

We now return to the scaling analysis of the spatial patterns shown in Figure 9. Consider the size scales plotted in the box-counting plots shown in the right column plot. The left-hand extreme of these plots matches the width of the screen: 1024 pixels (290mm), which corresponds to an angular motion of the eye of 29° . The right-hand extreme corresponds to 1 pixel (0.3mm), which corresponds to an angular motion of 0.03° . The arrow indicates the angle of 0.5° (5mm, 18 pixels on the screen) and corresponds to the expected cross-over size scale from motion dominated by saccades (small I/L scales) to motion dominated by micro-saccades (large I/L scales). At this size scale, we anticipate a ‘knee’ in the data since the two processes should exhibit different scaling properties.

Figure 9 therefore emphasizes the challenges of measuring limited-range fractals. At the left-hand extreme of the graph, the data follows $D = 2$ (as indicated by the fit line) because the limited number of boxes cannot distinguish the fractal trace from a filled space. At the left-hand extreme, the data follows $D = 1$ (as shown by the second fit line) because these small boxes sizes are approaching the data resolution limit and the analysis picks up the one-dimensional quality of the data line. This leaves a highly limited range of size scales (spanning two orders of magnitude) over which the data switches from one scaling behavior (saccades) to another (micro-saccades)! In terms of investigating the saccades, there is little flexibility for expanding the magnification range since the upper (fast frequency) cut-off is determined by the existence of micro-saccades (appearing at 0.5°). Only the lower cut-off (29°) could be improved by using a slightly bigger screen. However, at large angles of 65° and above, observers will start to search by using head-movement rather than eye-movement and this will provide a fundamental limit to the lower cut-off. Thus the observation range could be improved by only 0.5 orders.

Despite this limited range, we note the intriguing result that the effective dimension, determined from the slopes at large scales (i.e. the saccade behavior), appears to be insensitive to the D value of the fractal pattern being observed: the saccade pattern is quantified by $D = 1.4$, even though the underlying pattern varies over a very large range from 1.11 to 1.89. We also note that this characteristic value of $D = 1.4$ holds for observations of multi-colored fractals (bottom image). For comparison, we note the D

value expected for the spatial pattern (calculated using the temporal patterns' α value and using Equation 6) is $D = 1.25$.

To further test this result, we considered another form of fractal pattern for observers to search through – the computer-generated fractals shown in Figure 11.

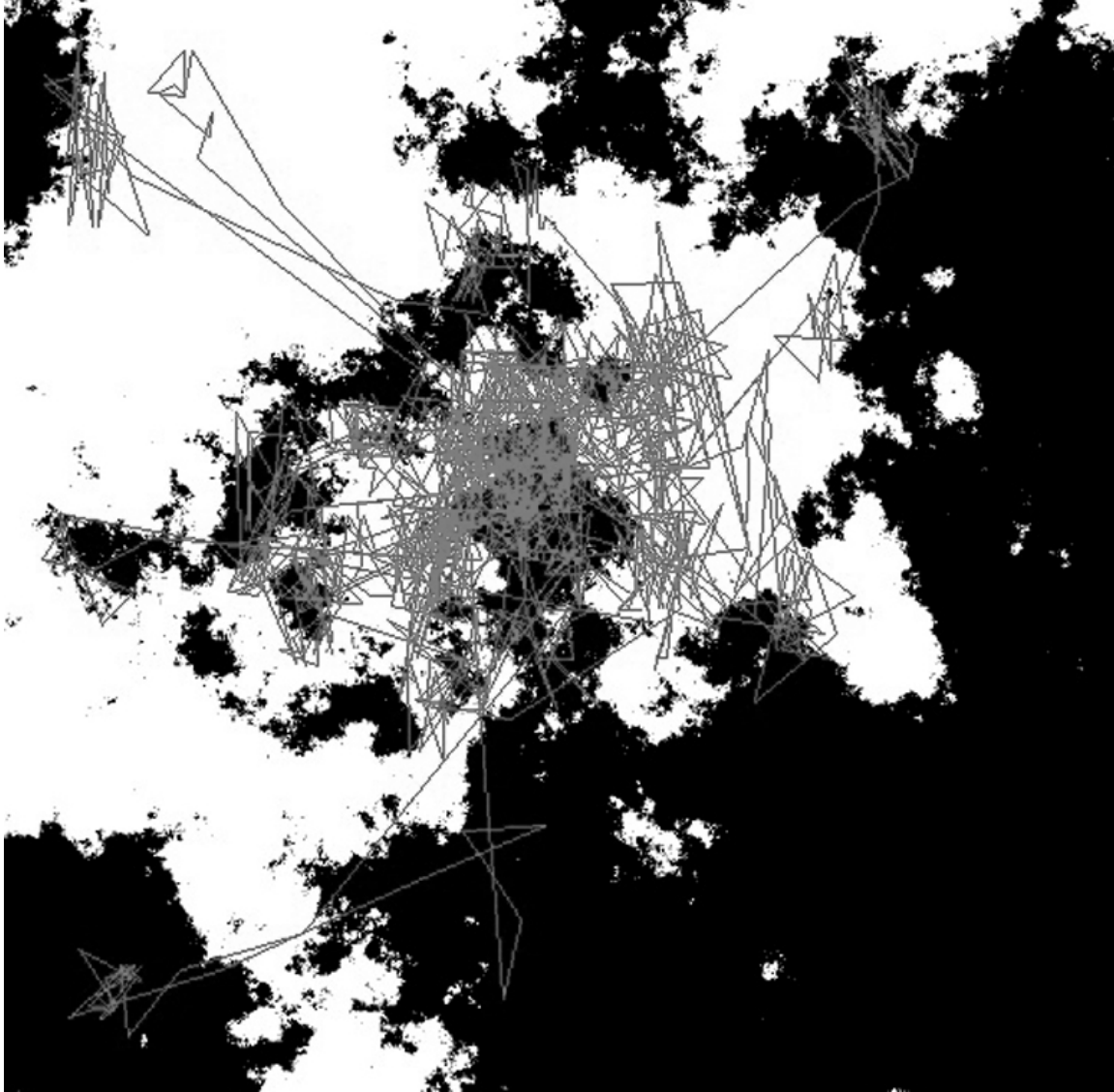


Figure 11. An example of the computer-generated fractals viewed by the subjects for the eye-tracking results shown in Table 3.

Table 3 compares the D values of the spatial patterns traced out by the saccades and the D values of the observed fractal patterns. In each case, the D values of the saccades are averaged over the results from 6 observers, each of whom observed the 9 fractal images for 30 seconds, separated by a checkerboard pattern observed for 30 seconds. Although preliminary, the results confirm that the saccades trace out an inherent search pattern set at $D = 1.5$, regardless of the scaling properties of the pattern being observed.

D image	D saccade
1.1	1.5
1.2	1.5
1.3	1.5
1.4	1.6
1.5	1.5
1.6	1.6
1.7	1.5
1.8	1.5
1.9	1.5

Table 3: A comparison of the D values of the fractal images being viewed, and the D values of the patterns traces out by the saccades.

4. Discussions/Conclusions

In this chapter, we have compared and contrasted two major forms of scaling analysis (power spectrum and box-counting analysis) and have applied them to the motions of the human eye - a physiological system that simultaneously generates temporal and spatial patterns. We will spend the remainder of the chapter discussing the implications of the results from this preliminary analysis.

Although the effective dimension of the saccade motion can only be charted over limited size scales, its insensitivity to such a wide range of D values in the observed pattern is striking. It suggests that the eye's search mechanism follows an intrinsic mid-range D value. Why would the eye adopt a fractal trajectory with a D value of 1.5? An appealing answer might lie in the mathematical properties highlighted in Figure 12. This Figure compares 3 trajectories quantified by different dimensions. The left hand image is that of a simple, straight line with $D = 1$. The right-hand image is a simulation of Brownian motion, in which a random process generates a trace with $D = 2$. The middle trace is a simulation of a fractal trace, with $D = 1.5$. This fractal trace is called a Levy flight, named after the mathematician who first developed their statistical qualities [13].

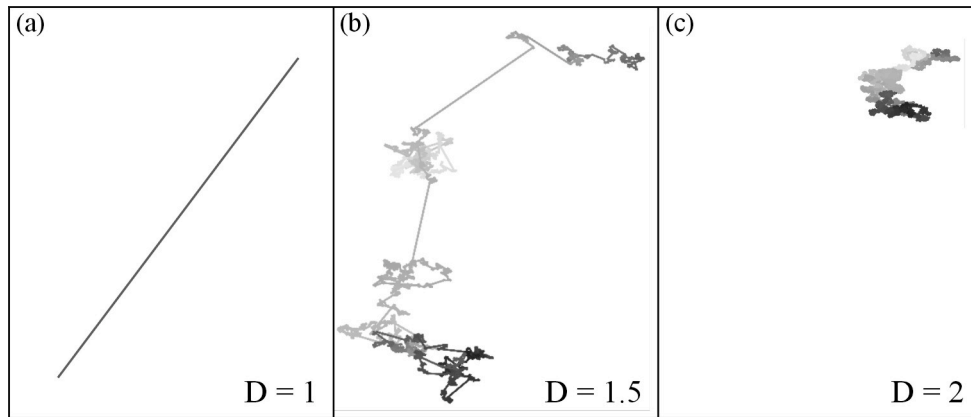


Figure 12. Potential search patterns, including (a) a single line of $D = 1$, (b) a Levy flight with $D = 1.5$, and (c) Brownian motion with $D = 2$.

Significantly, Levy flights were used to model the flights of the albatross in a pioneering experiment that measured the bird's foraging behavior across the Antarctic skies [14]. Although the model has recently been called into question [15], the experiment triggered a number of other investigations of foraging animals in which Levy flights were proposed to describe the animals behavior. Within this foraging model, the smaller trajectories allow the animal to look for food in small region and then to travel to neighboring regions and then onto regions further away.

Intriguingly, when the results of albatross investigations were first published, one of us (RPT) proposed that humans might subconsciously follow Levy flights when forced to cover vast spaces. The proposal was made within the context of artists, in particular for explaining how the abstract painter Jackson Pollock adopted his infamous pouring techniques to cover his epic (sometimes 30 foot wide) canvases with complex fractal patterns [16]. Recently, researchers have started to apply scaling analysis to cell phone data to examine if people also trace out fractal foraging behavior during their daily lives [17].

Significantly, the fractal flight has an enhanced diffusion compared to the equivalent random motion of a Brownian flight, and this might explain why it is adopted for search strategies. The Brownian flight lacks the longer flights of the fractal trace and thus its trajectories are confined within a small location, gradually filling space (hence the D value of 2). The enhanced diffusion of the fractal trace increases for smaller D values. The large amount of fine scale flights within a high D fractal causes the fractal to take on the characteristics of Brownian motion. In contrast, the low D fractals have a larger mix of long trajectories and these produce the enhanced diffusion. However, there is a limit to how small the D value should be. Although a trajectory of $D = 1$ has "enhanced" diffusion (the line in Figure 12(a) covers ground quickly), it doesn't explore much of the two-dimensional plane. It appears then that a mid-range D value might be optimal for covering terrain efficiently.

This provides an appealing explanation for why the human eye follows a fractal trajectory with an inherent D value set at 1.5 – the mathematics of its basic geometry dictate that it covers terrain efficiently when searching for information. This model raises

an obvious question – what happens when the eye is made to view a fractal pattern of $D = 1.5$? Will this trigger a ‘resonance’ when the eye sees scaling behavior that matches its own basic characteristics? Our previous research examining people’s perceptual and physiological responses to observing fractal patterns indicate a marked response when people observe mid- D fractals. This includes the reduction in physiological stress-levels of the observer [18, 19]. These results emphasize the important role of understanding the scaling properties of the human visual system.

Acknowledgments

We thank P. Van Donkelaar, C. Boydston and N. Kuwada at the University of Oregon for their help with the experimental investigations of the motion of the human eye. We thank A.P. Micolich and T.P. Martin for their helpful discussions on the analysis of fractal patterns. RPT was a Cottrell scholar of the Research Corporation during this project.

References

1. Goldberger, A.L., et al., *Fractal Dynamics in Physiology: Alterations with Disease and Aging*. Proceedings of the National Academy of Sciences, 2002. **99**: p. 2466 - 2472.
2. Taylor, R.P., *Chaos, Fractals, and Nature*. 1st ed. 2006, Eugene: Fractals Research.
3. Mandelbrot, B.B., *The Fractal Geometry of Nature*. 1982, San Francisco: W. H. Freeman. 460.
4. Bassingthwaighte, J.B., L.S. Liebovitch, and B.J. West, *Fractal Physiology*. 1994, New York: Oxford University Press. 364.
5. Bracewell, R.N., *The Fourier transform and its applications*. 3rd ed. 2000, Boston: McGraw Hill. 616.
6. Dubuc, B., et al., *Evaluating the fractal dimension of profiles*. Physical Review A, 1989. **39**(3): p. 1500 - 1512.
7. Berry, M.V. and Z.F. Lewis, *On The Weierstrass-Mandelbrot Fractal Function*. Proceedings of the Royal Society of London. Series A, Mathematical and Physical Sciences, 1980. **370**(1743): p. 459 - 484.
8. Barnsley, M.F., et al., *The Science of Fractal Images*, ed. H.-O. Peitgen and D. Saupe. 1988, New York: Springer-Verlag. 312.
9. Sprott, J.C., *Chaos and Time-Series Analysis*. 2003, New York: Oxford University Press. 507.
10. Hyona, J., et al., *The Brain's Eye: Neurobiological and Clinical Aspects of Oculomotor Research*. Progress in Brain Research. Vol. 140. 2002.
11. Aks, D.J., G.J. Zelinsky, and J.C. Sprott, *Memory Across Eye-Movements: 1/f Dynamic in Visual Search*. Nonlinear Dynamics, Psychology, and Life Sciences, 2002. **6**(1): p. 1 - 25.
12. Avnir, D., et al., *Is The Geometry of Nature Fractal?* Science, 1998. **279**: p. 39 - 40.

13. Taylor, R.P., *Levy Flights*, in *Encyclopedia of Nonlinear Science*, A. Scott, Editor. 2005, Routledge, Taylor & Francis Group: New York. p. 525 - 526.
14. Viswanathan, G.M., et al., *Levy flight search patterns of wandering albatrosses*. Nature, 1996. **381**: p. 413 - 415.
15. Edwards, A.M., et al., *Revisiting Levy flight search patterns of wandering albatrosses, bumblebees, and deer*. Nature, 2007. **449**: p. 1044 - 1048.
16. Taylor, R.P., A.P. Micolich, and D. Jonas, *Fractal Analysis of Pollock's Drip Paintings*. Nature, 1999. **399**: p. 422.
17. Gonzalez, M.C., C.A. Hidalgo, and A.-L. Barabasi, *Understanding individual human mobility patterns*. Nature, 2008. **453**: p. 779 - 782.
18. Taylor, R.P., *Reduction of Physiological Stress Using Fractal Art and Architecture*. Leonardo, 2006. **39**(3): p. 245 - 251.
19. Hagerhall, C.M., et al., *Investigations of human EEG response to viewing fractal patterns*. Perception, 2008. **37**(10): p. 1488 - 1494.